

CFD CALCULATION OF THE COMBUSTION AND RADIATION PROPERTIES OF LARGE-SCALE NATURAL GAS JET FLAMES

P.W.H.Barker, A.D.Johnson and N.Goto*

Shell Research Ltd., Thornton Research Centre, P.O. Box 1, Chester CH1 3SH.

© Shell Internationale Research Maatschappij B.V. 1995

The potential of Computational Fluid Dynamics (CFD) in the evaluation of fire hazard consequences is greater than that of empirical models based on experiments, since they incorporate models of the governing processes at a more fundamental level. As the first step towards the development of a validated CFD jet fire model, this paper describes the CFD-based calculation of the structure and radiation properties of large-scale horizontally released natural gas jet flames. Comparison is made between predictions and measurements taken from experiments.

KEYWORDS:

CFD modelling, Jet fire, Combustion, Thermal radiation

1. INTRODUCTION

Large-scale accidental jet fires, involving flammable, pressurised hydrocarbons, may pose a substantial hazard to personnel and property and can lead to escalation of an accident, particularly in congested areas. Quantification of the hazard is important if process plants and storage areas are to be designed and operated safely.

To date, computer packages used for the prediction of fire hazards do not directly model the small scale processes of fluid flow and turbulent combustion. Instead, scaling relations for physical parameters are generally formed from the global conservation laws of mass, momentum and heat balance. Key model constants are finally fixed by correlating with large-scale experimental data. Naturally, such models can be used confidently for predicting hazards from accidents similar to the large experiments on which they are based, but may become unreliable if used outside their experimentally validated range.

Advances in computer power and fundamental research over the last decade have made it feasible to directly model turbulent combustion phenomena using computational fluid dynamics (CFD). The incentive for this approach is that incorporation of detailed models of combustion chemistry, turbulent flow and radiative heat transfer, removes much of the dependence of the fire hazard models on expensive, large scale experiments. Instead, validation of the CFD turbulent combustion model can be made with smaller laboratory, or medium scale experiments, and then confidently extended to a larger scale or to more complicated release geometries. In addition, CFD calculations can provide insight for the development of new robust, simple-to-use, predictive tools.

* Tokyo Gas Trainee

This report presents recent work by Shell Research on a suite of combustion and radiation sub models for the CFD calculation of large-scale natural gas jet fires. The sub models are linked to the commercial solvers CFDS-FLOW3D and CFDS-RAD3D of AEA Technology, Harwell (1), which are used to provide domain gridding and to solve the turbulent transport and radiative heat transfer equations.

1.1. Characteristics of a natural gas jet fire

It is beneficial to have in mind an overall picture of a typical jet fire before we describe the individual sub models. Figure 1 highlights the essential features of a jet fire that a CFD calculation must succeed in modelling:-

1.1.1 Source If the stagnation drive pressure, $P_o > P_{atm} \left(\frac{1+\gamma}{2} \right)^{\gamma/(\gamma-1)}$, where γ is the ratio of specific heat capacities, the exit velocity is sonic and the orifice exit pressure is greater than atmospheric. On exiting, the jet rapidly expands and accelerates to supersonic speeds. Subsequent deceleration results in a normal shock a few source diameters downstream of the orifice, followed by a further series of expanding and reflected shock waves forming a diamond shock pattern.

1.1.2 Flame Lift-off The turbulent strain within and just downstream of the shock region is too violent to support a flame. If a flame tried to exist at a fuel/air interface, the rate at which heat and reaction radicals would be transported away by the flow far exceeds the generation rate, rapidly extinguishing it. Further downstream, these transport rates decrease to balance the generation rate and provide suitable conditions for a flame to exist. Flame lift-off greatly increases air entrainment into the initial part of the jet and must therefore be predicted accurately.

1.1.3 Turbulent Combustion Large eddies generated downstream by the turbulent flow entrain air which is mixed locally with the fuel by smaller eddies. Gaseous combustion occurs at a fuel/air interface. Unburnt fuel mixing with hot products is pyrolysed to form soot particles which at typical flame temperatures give the flame its characteristic yellow colour. Towards the end of the flame buoyancy forces begin to dominate and lift the flow. Unburnt soot escapes from the end of the flame, cools, and forms part of the thermal smoke plume.

1.1.4 Radiation At typical flame temperatures of 1500-1700K, the peak in the Planck spectrum overlaps strong absorption/radiation bands of water and carbon dioxide in the infra-red. These bands, together with the continuous radiation from any soot, chiefly contribute to the radiative heat transfer within the flame and to external objects. Approximately 20% of the released combustion energy is externally radiated from natural gas flames, reducing the peak temperatures from the adiabatic values in excess of 2000K, to approximately 1700K.

2. EXPERIMENTAL DATA

The experimental data used for the evaluation of the CFD calculations is taken from a series of large-scale natural gas jet flames carried out jointly with British Gas from 1987 to 1990 (2), and partly funded by the European Community. We choose a high pressure release (stagnation pressure is 67.1 bara) to compare with our predictions. The orifice conditions are given in Table 1. The flame exhibits all of the features

described above. Side-on profiles of the flame were recorded on video and the flame image digitally analysed off-line after each test. For each video frame, the image analyser scans each pixel and records a positive count if the intensity of the primary colour red exceeds a low threshold value. A percentage occurrence image can be constructed after sampling many frames, see figure 5a), and is, in effect, the footprint of the hot radiating soot. The lift-off length fluctuated between 1.6 and 2.0m, and was followed by a blue flame. The yellow region of the flame started approximately 8.0m downstream.

3. TURBULENT COMBUSTION CHEMISTRY

Accurate prediction of the flame characteristics and external radiation hazards require a turbulent combustion model with sufficient complexity to capture the experimental observations of flame lift-off, soot production and external radiation. At one end of the spectrum, the mixed-is-burnt model stoichiometrically burns the mixed fuel and air to carbon dioxide and water, but does not include the effect of the turbulent intensity on the combustion. At the other end, direct numerical calculation of turbulent combustion, in which kinetic models for multi-species, multi reaction chemistry are incorporated into the turbulent fluctuating fluid motions, is beyond the capabilities of current computers for all but the simplest flows. At present a compromise between the two extremes is usually adopted.

The combustion of a high pressure jet is commonly viewed as predominantly non-premixed, although the extent of non-premixed versus premixed combustion (especially just after the lift-off region) has recently been raised in the literature (3). We base our modelling on non-premixed combustion and couple it to the degree of fuel/air mixing by the underlying flow field, through a conserved scalar, the mixture fraction f . The mixture fraction is normalised to vary between, $f = 1$ for fuel and $f = 0$ for oxidant (pure air). The extent of the turbulent mixing of fuel and air is given by a value of f in-between 0 and 1, which then uniquely specifies the instantaneous combustion properties (species composition, heat release, temperature etc.). Turbulent fluctuation effects on the combustion properties are incorporated by assuming that the statistical variation in the mixture fraction can be modelled using a probability density function (PDF) of a presumed shape. A PDF constructed from a beta function is commonly used which can be fully prescribed at each location in terms of the mixture fraction mean \bar{f} and its variance g . Turbulent transport equations are solved for these two variables,

The principle advantage of this approach is that the mixture fraction is conserved throughout the reaction zone, so that there are no difficult to solve chemical reaction source terms in the transport equations, which allows the chemistry to be calculated off-line and stored in look-up libraries. There are various ways of determining the instantaneous non-premixed flame composition as a function of the mixture fraction, depending on the assumptions about the form of the flame and whether the flame composition is taken to depend on other independent variables. We assume the turbulent diffusion flame is locally and instantaneously an ensemble of strained laminar diffusion flamelets (SLF). The hydrodynamic strain stretches each flamelet and inhibits radicals from diffusing to the reaction zone. The combustion heat release rate is reduced as the strain rate increases, until at sufficiently high strain rate the flame extinguishes and isothermal mixing occurs. The high strain rates close to the orifice of a jet release extinguish the flame to produce the characteristic flame-lift off.

The composition of each SLF is taken to depend on the instantaneous mixture fraction and strain rate in the same way as it does in a counter flow laminar diffusion flame, formed by the combustion of two opposed jets, one containing air, the other fuel. The combustion chemistry is therefore calculated off-line from models of counterflow strained laminar diffusion flames.

3.1. Counter flow diffusion flames - RUN-1DL

The computer program RUN-1DL (4) from Cambridge University Engineering Department is used to obtain the structure and combustion properties of counter flow laminar diffusion flames. Full chemical kinetics, detailed transport and thermodynamic properties are provided by the CHEMKIN-II code from Sandia Laboratories (5).

3.1.1. Flow geometry and definition of strain rate, s The opposed planar fuel and air jets are shown in figure 2. The fuel source is located at $x = 0, y = -\infty$ and the air source is located at $x = 0, y = +\infty$ (In practice the source streams occur at finite values of y but sufficiently far apart to not affect the calculated properties). In this report the strain rate is defined as the velocity gradient in the x -direction, given by the following expression,

$$s = \frac{\partial u}{\partial x} \quad (1)$$

and as $y \rightarrow \infty$ we have $u(x, \infty) = u_o(x) = s_o x$. Standard 2-dimensional boundary layer equations are solved for continuity, momentum, energy and species, with similarity transformation further simplifying them to 1-dimension.

3.1.2. Elementary reaction scheme The chemical mechanism used for the calculation of the reaction rates for counterflow methane air diffusion flames incorporates 78 elementary reactions for 27 species in order to predict the formation of C_2H_2 , a soot precursor which has successfully been used in the modelling of soot formation in turbulent natural gas and propane diffusion flames. The C_2 reaction mechanism has been derived from a scheme published by Peters (6), with modifications from Baulch *et al.*, (7). The accuracy of the scheme has been tested by calculation of the laminar premixed flame speed, 0.43m/s at stoichiometric conditions, and comparison with measurements on a porous burner show that the predictions of the acetylene and other species concentrations are good.

3.2. Prescription of the mixture fraction, f

Consider a two stream fuel/air mixing process. Any extensive property f of the mixture can be written in terms of the pure fuel and pure air properties as, $f = x f_f + (1-x) f_a$, where x is the fuel mass fraction. Such extensive properties, which do not have sinks or sources during the mixing process, are termed *conserved properties*.

The conserved scalar prescribing the mixture fraction is given by Bilger (8) for fuels containing carbon and hydrogen only,

$$f = \frac{\frac{2Y_c}{M_c} + \frac{1}{2} \frac{Y_H}{M_H} + \frac{(Y_{o,o} - Y_o)}{M_o}}{\frac{2Y_{c,f}}{M_c} + \frac{1}{2} \frac{Y_{H,f}}{M_H} + \frac{Y_{o,o}}{M_o}} \quad (2)$$

where Y_i is the mass fraction of the element i , M_i is the atomic weight of element i . $Y_{i,o}$ is the mass fraction of element i in the oxidant and $Y_{i,f}$ is the mass fraction of element i in the fuel. Note $f = 1$ in the fuel stream and $f = 0$ in the oxidant stream.

Strained laminar flamelets have been calculated in a planar geometry using the C_2 chemistry for strain rates ranging from $s = 2 \text{ s}^{-1}$ to the extinction strain rate of $s = 504.2 \text{ s}^{-1}$, at which point the flow field carries the important combustion radicals O, H and OH, away from the reaction zone faster than they can be generated, extinguishing the flame to leave only isothermal mixing. Figure 3 shows the adiabatic temperature profiles along the y-axis for increasing values of the strain rate. The laminar flame sits on the air side of the stagnation point but as the strain rate increases the peak flame temperature decreases, it moves towards the fuel side and the flame width narrows. At a fixed strain rate the y position can be expressed in terms of a unique value of the mixture fraction as in Figure 4, where the adiabatic temperature is plotted against mixture fraction for a strain rate of 100 s^{-1} and also for one close to extinction. In both cases, the peak temperature occurs close to the stoichiometric value of the mixture fraction $f_{st} = 0.056$, but is reduced by almost 300K for the high strain rate flamelet. Comparisons of temperature and species profiles with other calculations in the literature are favourable, especially for the intermediate acetylene which is used as precursor in the soot modelling.

Finally, from the profile in Figure 4 and similar ones, look-up tables are compiled for species mass fractions, adiabatic temperature, adiabatic density, adiabatic thermal enthalpy, specific heat capacity and volumetric heat release rate as functions of the independent variables mixture fraction f and strain rate s .

4. FLAME LIFT-OFF

In the experimental sonic jet flame the first flame existence appears as a bluish flame between 1.5 and 2.0m downstream of the orifice. Preliminary calculations indicated that the mean strain rate at this position is much greater than the extinction rate for strained laminar diffusion flames. An explanation of this observation is that the initial flame is a near stoichiometric pre-mixed flame, which can exist at higher strain rates than diffusion flamelets. The bluish appearance, characteristic of a pre-mixed flame, also adds weight to this. Recent work by Gu (9) has predicted the lift-off height for laboratory scale natural gas flames using pre-mixed flamelets, and finds good agreement with experiment.

In our work, we have therefore adapted Gu's results to provide a lift-off criterion based on pre-mixed flamelets, but after which the flame is then an ensemble of diffusion flamelets. This is necessary at the moment because the calculations performed by Gu did not include soot formation or thermal radiation. A future objective is to develop suitable pre-mixed flamelet libraries.

Gu's work is based on the theory developed by Bradley *et al.*, (10) that a flame can only survive at a particular position if the average volumetric heat release exceeds a certain threshold. The average premixed volumetric heat release rate is given by,

$$\bar{q} = \int_{f_{\min}}^{f_{\max}} P_b(f) \int_0^1 q_i(\theta, f) p(\theta, f) d\theta df \quad (3)$$

where θ is a non-dimensional reaction progress variable, which varies from 0 to 1 through the flame, $q_i(\theta, f)$ is the laminar heat release rate, $p(\theta, f)$ is the joint pdf, $P_b(f)$ is the probability that the local mean turbulent strain rate is sufficiently low to permit flamelets to burn and f_{\min} and f_{\max} are the mixture fractions corresponding to the upper and lower flammability limits. $P_b(f)$ is expressed as a simple function of the Karlovitz stretch factor,

$$K = \left(\frac{\epsilon v}{15} \right)^{0.5} \frac{1}{u_i^2(f)} \quad (4)$$

and the Lewis number $Le (= 0.975)$, where ν is the kinematic viscosity ($1.5 \times 10^{-5} \text{ m}^2\text{s}^{-1}$), ϵ is the turbulent dissipation rate and $u_l(f)$ is the laminar flame speed.

Gu's results show that the lift-off point for a natural gas flame occurs on the mean stoichiometric mixture fraction contour at a point where the mean turbulent heat release rate is $\bar{q} = 3.0 \text{ MW/m}^3$. Since we are unable to define a reaction progress variable for our diffusion flamelet based calculations, the crude assumption is made that, on the mean stoichiometric mixture fraction contour near the lift-off point,

$$\bar{q} \propto P_b(\bar{f}) \quad (5)$$

Consideration of the calculated laboratory scale turbulent mean strain rate in terms of the rms turbulent velocity u' and the Taylor lengthscale λ ,

$$\frac{u'}{\lambda} = \left(\frac{\epsilon}{15\nu} \right)^{0.5} \quad (6)$$

implies that, at the lift-off point, $P_b(\bar{f}) \approx 0.3$. We therefore determine our flame lift-off position by searching close to the stoichiometric mean mixture fraction contour and moving closer to the orifice until the value of P_b falls below 0.3. For values of P_b below this, the fuel and air isothermally mix in the flame-lift off region instead of burning.

5. SOOT MODELLING

It is possible to specify the gaseous combustion chemistry in terms of instantaneous flow field variables because the time scale on which the combustion occurs is much smaller than the shortest time scale of the flow. However, soot chemistry is much slower than gaseous chemistry with a time scale comparable to the flow, and means that transport equations must be solved for the soot evolution. Fairweather *et al.* (11) have successfully modelled the soot evolution in vertical, subsonic natural gas flames using a soot chemistry scheme due to Lindstedt (12). The model takes the presence of the combustion species acetylene to govern the propensity of soot to form. Turbulent transport equations are written for the soot mass fraction Y_s and the soot number density, N . We have incorporated the same model into our work for sonic, horizontal flames and only list the main features. Full details of the scheme and turbulent transport equations to solve are given in reference (11).

The transport equation for soot mass fraction contains source terms for nucleation R_{nucI} , surface growth R_{surf} and a sink term for destruction via oxidation R_{ox} . The formation of carbon nuclei from acetylene follows from the reaction, $C_2H_2 \Rightarrow 2C + H_2$. This process is followed by initial formation of soot particles which must contain a minimum of 9×10^4 carbon atoms. An activation temperature of 21,000K is needed for the nucleation step giving,

$$R_{nucI} = k_1(T)[C_2H_2]$$

with $k_1(T) = 1.36 \times 10^6 \exp\left(-\frac{21000}{T}\right)$ (7)

Soot mass growth is assumed to proceed by the adsorption of acetylene molecules at the surface of each particle and is presumed to be first order in acetylene concentration. To account for the experimental observation that soot particle ageing reduces surface reactivity it is assumed that the number of active sites

present locally in the flame is proportional to the square root of the total area S available. The reaction source term is given by,

$$R_{surf} = k_2(T)S^{1/2} [C_2H_2]$$

with $k_2 = 5.0 \times 10^2 \exp\left(-\frac{12100}{T}\right)$ (8)

The soot oxidation follows the expression formulated by Lee *et al.*, (13). It is assumed that solid carbon is exclusively oxidised over the soot surface area to form carbon monoxide at typical flame temperatures, and only by molecular oxygen,

$$R_{ox} = k_3S [O_2]$$

$k_3(T) = 1.78 \times 10^4 \sqrt{T} \exp\left(-\frac{19680}{T}\right)$ (9)

There is one source term and one sink term in the transport equation for soot number density. The source is a direct consequence of the soot nucleation term and the sink term accounts for a decrease in the number density from soot agglomeration.

6. RADIATIVE HEAT TRANSFER

Radiative heat transfer plays an integral part in the modelling of a combusting system. It shares an equal role with convection for the transfer of heat within a turbulent diffusion flame, but is entirely responsible for the radiation emanating from the flame which is incident on external objects. Radiative heat transfer is a demanding calculation because many coupled processes contribute. For example, at a particular position within a flame the local cooling due to the loss of radiative heat depends on the local absorption coefficient and the local temperature. However, the local temperature partly depends on the local heating from absorbed radiation which has emanated from other regions of the flame. The absorption coefficient is related to the local mass fractions of carbon dioxide, water vapour and soot which themselves depend partly on the local temperature. Clearly, iterative numerical techniques are needed to calculate the radiative heat transfer in such systems.

The sister code RAD3D provides two methods for the radiative heat transfer calculation, the Discrete transfer model (14) which calculates energy transfer along pre-defined rays fired from surfaces and the Monte Carlo model which traces the histories of simulated packets of photons. Unless special pseudo-surfaces are specified, the discrete transfer method propagates rays from solid surfaces and the boundaries of the computational domain. The CFDS-FLOW3D domain for open-air flames is large compared with the flame volume, thus a large proportion of the rays from the boundaries would be wasted since they do not pass through the flame. The Monte Carlo method is more efficient for a free flame problem, and is the one we use, because the photon packets originate from areas of high luminosity, *id est.*, inside the flame. They immediately sample the absorption/emission characteristics of the flame and then, if they survive, travel to outer boundaries where they contribute to external radiation.

RAD3D divides the space into connected zones and the outer boundaries are divided into surface panels. A RAD3D zone may envelope several CFDS-FLOW3D cells and a representative zone temperature T_z and zone absorption/emission coefficient k_z are calculated from the contributing CFDS-FLOW3D cells in a way to maintain energy conservation. RAD3D performs the Monte Carlo algorithm and returns the net radiative heating Q_{rad} within each CFDS-FLOW3D cell as a source term in the thermal enthalpy transport equation.

A good account of the Monte Carlo algorithm is in reference (1), here we outline the construction of the absorption/emission coefficients. A typical combustion product mixture of CO_2 and H_2O contains many vibrational transitions with corresponding absorption lines in the infrared region. The profile consists of many close packed lines which are grouped into bands with perfect transmission windows in between. For a particular band we construct the band transmissivity over a distance l , representative of the zone size, of all the lines within it,

$$\tau_{band}(l) = \frac{1}{\Delta\omega} \int_{lines} e^{-\int k_{\omega}(\omega') d\omega'} d\omega \quad (10)$$

where $\Delta\omega$ is the band width. In order to calculate this integral the line absorption coefficient k_{ω} is approximated by an analytic form using the Edwards wide band model (15). The absorption lines are reordered with the band so that the strongest is at the centre and the strengths of the others fall off as you move either side of it. An exponential band shape is then fitted to this reordered spectrum giving,

$$k_{\omega} = \frac{\alpha}{\omega^*} e^{-\left| \frac{\omega - \omega_0}{\omega^*} \right|} \quad (11)$$

where ω_0 is the band centre, ω^* is the band width and α is the total band intensity. Further work is still needed to evaluate the integral and several approximations have been constructed by Cess and Tiwari (16), and Goody and Belton (17).

Absorption cross sections for soot particles can be calculated using classical Mie theory. The diameter of the soot particles is sufficiently small that the Rayleigh approximation holds to give a soot absorption coefficient inversely proportional to the incoming radiation wavelength λ , and not a grey emitter as it is commonly mistaken to be,

$$k_{soot} = 36\pi f_v \phi / \lambda \quad (12)$$

where f_v is the soot volume fraction and,

$$\phi = n^2 k / [(n^2 + n^2 k^2)^2 + 4(n^2 - n^2 k^2 + 1)] \quad (13)$$

a function of the complex refractive index, $\hat{n} = n(1 - ik)$.

Although banded radiation calculations can be performed using RAD3D we use grey gas absorption coefficients. In the flame it is assumed the radiative heat transfer is in equilibrium and that the emission coefficient equals the absorption coefficient at the local flame temperature. The combined gas and soot transmissivities of the bands is weighted by the area under the Planck spectrum the band overlaps to give an overall transmissivity for a path length l ,

$$\tau(l) = \frac{1}{\sigma T^4} \sum_{bands} f_{band}(T) \tau_{band}(l) \tau_{soot}(l) \quad (14)$$

where,

$$\tau_{soot}(l) = \frac{1}{\Delta\omega} \int_{band} e^{-(36\pi f_v \phi / \lambda) l} d\omega \quad (15)$$

and $f_{band}(T)$ is the fraction of the area underneath the Planck spectrum at the local flame temperature that overlaps the band. From this the grey gas absorption/emission coefficient is follows as,

$$k = -\frac{1}{f} \ln(1 - \tau(f)) \quad (16)$$

The air outside of the flame is not in radiative equilibrium and therefore it is not strictly correct to assign it equal absorption and emission coefficients. However, it is more important to accurately model the absorption of flame radiation by the air, than it is to account for the small contribution of the air to the total radiative emission. In the air, k is set equal to the absorption coefficient which is obtained in the same manner, except that a representative flame temperature is now used instead of the local air temperature.

The simulations described in this paper do not incorporate a fully coupled combustion and radiation calculation where at each iteration the flame temperature is adjusted to match the calculated radiative heat loss. Instead, the flame temperature is pre-adjusted off-line to account for radiative heat loss using the approach of Crauford et al. (18),

$$T(f) = T_{ad}(f) [1 - 0.15(T_{ad}(f) / T_{ad,max})^4] \quad (17)$$

where $T_{ad}(f)$ is the adiabatic flamelet temperature. The density is adjusted using the ideal gas law. Radiative heat fluxes to objects outside the flame are then calculated as a post-process after the flow solution has converged. Future simulations will include the coupled effect of radiative energy exchange and combustion via the energy equation.

7. FLOW3D SOLUTION PROCEDURE

A simple 3-d rectangular grid is sufficient for simulation of free natural gas flames modelled as horizontal releases in the x-direction. The gridding is not uniform but is refined close to the fuel inlet and along the jet axis where the highest velocity gradients exist. The lower x-plane contains an inlet patch for the fuel stream on which appropriate boundary conditions are enforced for the transport equations. The ground is on the lower y-plane at $y=0$. Remaining boundaries at the edge of the domain are either inlet patches representing any wind inflow or pressure boundaries set to atmospheric pressure. Atmospheric boundary layer profiles are used to specify the wind profiles.

CFDS-FLOW3D solves for continuity and turbulent transport equations for the mean velocities together with the above transport equations required for the combustion (mixture fraction and variance), soot (soot mass fraction and soot number density) and radiation (thermal enthalpy). The Favre averaged form is used for the transport equations and are closed using the standard k - ϵ turbulence. The numerical solutions are obtained from steady state calculations. A few thousand iterations may be required for convergence (mass residuals $< 0.1\%$). Because of their central role in prescribing the combustion, the inner equations for mixture fraction and its variance should be swept several times per iteration to keep the convergence on track. 'Hybrid' difference schemes are used for the convective term in the transport equation. After the combustion calculation has converged, the radiative heat transfer calculation is performed once as a post-process to determine the external radiation.

As a test of the combined potential of the combustion, soot, lift-off and radiation sub models we focus on the modelling of the experimental sonic natural gas jet and show the results of recent development work on a full modelling of the shock structure compared with a simple model for the jet source.

7.1. Simple jet source model

There are a number of algebraic models for the calculation of the expansion of high pressure gas jets. The models incorporate continuity, momentum and energy balances to expand the jet down to atmospheric pressure. Although they prescribe the flow variables at the atmospheric pressure plane, they cannot predict the downstream distance where the plane is positioned. Flame lift-off lengths and total flame lengths will be under-predicted if this is not accounted for. We test the model of Birch *et al.*, (19) which expands the jet to atmospheric pressure at the speed of sound and at ambient temperature, without entraining air. The properties are uniform across the jet leaving the jet diameter uniquely determined. The final parameters for the jet inlet in the CFDS-FLOW3D calculation are given in Table 1. The jet source turbulence is set to typical values for fully developed flow in pipes.

7.2. Resolving the shock structure

The alternative is to fully calculate the jet expansion using CFDS-FLOW3D. The high grid resolution required to resolve the shock structure forces the jet expansion to be performed on a much smaller scale, as a pre-calculation to the combustion one. The axisymmetry of the expanding jet reduces the computation to 2 dimensions which solves the same transport equations (except soot) as above. The sonic flow must be treated as fully compressible and solved as a transient calculation. The optimum grid size is $100 \times (\text{pipe diam})$ in the downstream direction, covered by 150 cells, and $10 \times (\text{pipe diam})$ radially, covered by 60 cells. Adaptive time stepping is used at the start to determine the initial time step which is of the order $10^{-6} - 10^{-7} s$. Development work compared predictions with experimental data of Birch *et al.* on under-expanded air jets. Good agreement is found when the turbulent viscosity is reduced by decreasing C_μ in the k- ϵ model from 0.09 to 0.06. In effect, this is a partial cure for the over-spreading of a round jet in k- ϵ calculations. For the sonic natural gas flame, the inlet conditions at the orifice are shown in Table 1.

Finally, a line slice of the 2-d flow structure is taken after the jet has fully expanded and is mapped onto an inlet patch of a large 3-d grid for the full combustion calculation.

8. RESULTS AND DISCUSSION

8.1. Shock Front Resolution

Figure 6 shows the Mach number profile close to the nozzle during the expansion of the high pressure jet. The picture is a half slice along the jet centreline and should be reflected about the bottom plane for a full view. The gas accelerates to supersonic velocities shortly after the nozzle. Interaction of the shock waves forms a characteristic barrel structure with a normal shock at the front. The flow in the central core rapidly slows after the normal shock but also flows at high speed around the outside in regions known as 'slip lines'.

8.2. Flame calculation

The radial slice is taken across the jet at a downstream distance of 1.4m, where the maximum Mach No. approaches 0.3, and is mapped onto an inlet patch for the flame calculation. The predicted flame lift-off is approximately 2.0m which compares well with observation, but the flame trajectory is slightly more buoyant than the experimental one. For the full source term calculation, figure 8 shows good predictions of cross-stream jet temperatures compared with thermocouple measurements at selected downstream planes.

8.3. Soot profile

Figure 5b) shows the soot footprint, the soot number density N , produced by the combustion calculation and is the best candidate for a direct comparison with the image analysis picture. The term flame length usually refers to the average length visible to the naked eye, *id est*, what the image analyser sees. The centreline distance to the point where the soot profile rapidly decreases is therefore the best CFD estimate of the flame length. Comparison of figure 5b) with the image analysis shows the agreement is good. The predicted centreline temperature, figure 7, remains high after the end of the visible flame and is therefore not a reliable indicator.

Figure 5c) shows the soot number density profile for the calculation using the simple jet source. As expected, the flame lift-off is less than the experimental observation, although the flame trajectory and visible length show good agreement. The simpler source term also gives a flatter trajectory and less jet spreading than the full shock calculation.

8.4. External radiation

The maximum soot volume fraction levels are of the order 10^{-8} , and are too low to significantly contribute to the external heat radiation. This is reflected in the external radiation calculations which show that the water vapour and carbon dioxide are solely responsible for the recorded intensities. Table 2. shows the positions of 4 radiometers with the measured and predicted incident fluxes. There is little variation between the predicted fluxes from either calculation which compare well with measurements.

9. CONCLUSIONS

1. We have successfully modelled the shock structure for a high pressure natural gas release. This provides an accurate source term necessary for the jet lift-off prediction and downstream combustion.
2. The predicted soot profiles, particularly length, correspond well with the experimental visible flame.
3. Flame trajectory, soot concentrations and external radiation all show good agreement with experiment.
4. The successful validation of the CFD package makes it a powerful tool in the future of hazard consequence modelling.

10. REFERENCES

1. FLOW3D Release 3.3, 1994, User Manual, CFD Department AEA Industrial Technology, and C. Hesketh and P.W. Guilbert, 1989, "RAD3D user manual Version 1.2", AERE-R 13710, HCCP/R32/1989.
2. J. N. Davenport, J.F. Bennett, L.T. Cowley and J.J. Rowson, 1991, "Large-scale natural gas and LPG jet fires. Final report to the CEC", TNER 91, publ. Shell Research Ltd.
3. D. Bradley, P.H. Gaskell and A.K.C. Lau, 1990, "A mixedness-reactedness flamelet model for turbulent diffusion flames", 23rd Symposium on Combustion, pp. 685-692.
4. B. Rogg, 1993, "RUN-1DL. The Cambridge Universal Laminar Flame Code. Version 11.1".
5. R.J. Kee, F.M. Rupley and J.A. Miller, 1991, "CHEMKIN-II: A fortran chemical kinetics package for the analysis of gas phase chemical kinetics", Sandia Report SAND89-8009B.
6. N. Peters, 1984, "Laminar diffusion flamelet models in non-premixed turbulent combustion", Prog. Energy and Combust. Sci., 10, pp. 319-339.
7. D.L. Baulch, C.J. Cobois, R.A. Cox, C. Esser, P. Frank, Th Just, J.A. Ferr, M.J. Pilling, J. Troe, R.W. Walker and J. Warnatz, 1992, "Evaluated kinetic data for combustion modelling", J. Phys. Chem. Ref. Data, 21, no.3, pp411-429.
8. R.W. Bilger, 1988, "The structure of turbulent non-premixed flames", 22nd Int. Symp. on Comb., pp 475-488.
9. X. J. Gu, 1994, Ph.D thesis, Leeds University.
10. D. Bradley, P. H. Gaskell and X. J. Gu, 1994, "Applications of a Reynolds Stress, stretched flamelet, mathematical model to computations of turbulent burning velocities and comparison with experiments", Comb. and Flame 96:221-248.
11. M. Fairweather, W.P. Jones and R.P. Lindstedt, 1992, "Predictions of radiative heat transfer from a turbulent reacting jet in a cross-wind", Combustion and flame, 89, p 45.
12. K.M. Leung, R.P. Lindstedt and W.P. Jones, 1991, "A simplified reaction mechanism for soot formation in nonpremixed flames", Comb. and Flame, 87, pp 289-305.
13. K.B. Lee, M.W. Thring, J.M. Beer, 1962, Combustion and Flame, 6, p137.
14. F.C. Lockwood and N.G. Shah, 1981, "A new radiation solution method for incorporating in general combustion prediction procedures", 18th Int. Symp. on Comb., p1405.
15. D.K. Edwards and A. Balakrishnan, "Thermal radiation by combustion gases", Int. J. Heat Mass Transfer, Vol. 6, p25-40.
16. R.D. Cess, and S. N. Tiwari, 1972, "Infrared radiative energy transfer in gases", Advances in Heat Transfer, Vol. 8, pp. 229-283.

8.2. Flame calculation

The radial slice is taken across the jet at a downstream distance of 1.4m, where the maximum Mach No. approaches 0.3, and is mapped onto an inlet patch for the flame calculation. The predicted flame lift-off is approximately 2.0m which compares well with observation, but the flame trajectory is slightly more buoyant than the experimental one. For the full source term calculation, figure 8 shows good predictions of cross-stream jet temperatures compared with thermocouple measurements at selected downstream planes.

8.3. Soot profile

Figure 5b) shows the soot footprint, the soot number density N , produced by the combustion calculation and is the best candidate for a direct comparison with the image analysis picture. The term flame length usually refers to the average length visible to the naked eye, *id est*, what the image analyser sees. The centreline distance to the point where the soot profile rapidly decreases is therefore the best CFD estimate of the flame length. Comparison of figure 5b) with the image analysis shows the agreement is good. The predicted centreline temperature, figure 7, remains high after the end of the visible flame and is therefore not a reliable indicator.

Figure 5c) shows the soot number density profile for the calculation using the simple jet source. As expected, the flame lift-off is less than the experimental observation, although the flame trajectory and visible length show good agreement. The simpler source term also gives a flatter trajectory and less jet spreading than the full shock calculation.

8.4. External radiation

The maximum soot volume fraction levels are of the order 10^{-8} , and are too low to significantly contribute to the external heat radiation. This is reflected in the external radiation calculations which show that the water vapour and carbon dioxide are solely responsible for the recorded intensities. Table 2. shows the positions of 4 radiometers with the measured and predicted incident fluxes. There is little variation between the predicted fluxes from either calculation which compare well with measurements.

9. CONCLUSIONS

1. We have successfully modelled the shock structure for a high pressure natural gas release. This provides an accurate source term necessary for the jet lift-off prediction and downstream combustion.
2. The predicted soot profiles, particularly length, correspond well with the experimental visible flame.
3. Flame trajectory, soot concentrations and external radiation all show good agreement with experiment.
4. The successful validation of the CFD package makes it a powerful tool in the future of hazard consequence modelling.

10. REFERENCES

1. FLOW3D Release 3.3, 1994, User Manual, CFD Department AEA Industrial Technology, and C. Hesketh and P.W. Guilbert, 1989, "RAD3D user manual Version 1.2", AERE-R 13710, HCCP/R32/1989.
2. J. N. Davenport, J.F. Bennett, L.T. Cowley and J.J. Rowson, 1991, "Large-scale natural gas and LPG jet fires. Final report to the CEC", TNER 91, publ. Shell Research Ltd.
3. D. Bradley, P.H. Gaskell and A.K.C. Lau, 1990, "A mixedness-reactedness flamelet model for turbulent diffusion flames", 23rd Symposium on Combustion, pp. 685-692.
4. B. Rogg, 1993, "RUN-IDL. The Cambridge Universal Laminar Flame Code. Version 11.1".
5. R.J. Kee, F.M. Rupley and J.A. Miller, 1991, "CHEMKIN-II: A fortran chemical kinetics package for the analysis of gas phase chemical kinetics", Sandia Report SAND89-8009B.
6. N. Peters, 1984, "Laminar diffusion flamelet models in non-premixed turbulent combustion", Prog. Energy and Combust. Sci., 10, pp. 319-339.
7. D.L. Baulch, C.J. Cobois, R.A. Cox, C. Esser, P. Frank, Th Just, J.A. Ferr, M.J. Pilling, J. Troe, R.W. Walker and J. Warnatz, 1992, "Evaluated kinetic data for combustion modelling", J. Phys. Chem. Ref. Data, 21, no.3, pp411-429.
8. R.W. Bilger, 1988, "The structure of turbulent non-premixed flames", 22nd Int. Symp. on Comb., pp 475-488.
9. X. J. Gu, 1994, Ph.D thesis, Leeds University.
10. D. Bradley, P. H. Gaskell and X. J. Gu, 1994, "Applications of a Reynolds Stress, stretched flamelet, mathematical model to computations of turbulent burning velocities and comparison with experiments", Comb. and Flame 96:221-248.
11. M. Fairweather, W.P. Jones and R.P. Lindstedt, 1992, "Predictions of radiative heat transfer from a turbulent reacting jet in a cross-wind", Combustion and flame, 89, p 45.
12. K.M. Leung, R.P. Lindstedt and W.P. Jones, 1991, "A simplified reaction mechanism for soot formation in nonpremixed flames", Comb. and Flame, 87, pp 289-305.
13. K.B. Lee, M.W. Thring, J.M. Beer, 1962, Combustion and Flame, 6, p137.
14. F.C. Lockwood and N.G. Shah, 1981, "A new radiation solution method for incorporating in general combustion prediction procedures", 18th Int. Symp. on Comb., p1405.
15. D.K. Edwards and A. Balakrishnan, "Thermal radiation by combustion gases", Int. J. Heat Mass Transfer, Vol. 6, p25-40.
16. R.D. Cess, and S. N. Tiwari, 1972, "Infrared radiative energy transfer in gases", Advances in Heat Transfer, Vol. 8, pp. 229-283.

8.2. Flame calculation

The radial slice is taken across the jet at a downstream distance of 1.4m, where the maximum Mach No. approaches 0.3, and is mapped onto an inlet patch for the flame calculation. The predicted flame lift-off is approximately 2.0m which compares well with observation, but the flame trajectory is slightly more buoyant than the experimental one. For the full source term calculation, figure 8 shows good predictions of cross-stream jet temperatures compared with thermocouple measurements at selected downstream planes.

8.3. Soot profile

Figure 5b) shows the soot footprint, the soot number density N , produced by the combustion calculation and is the best candidate for a direct comparison with the image analysis picture. The term flame length usually refers to the average length visible to the naked eye, *id est*, what the image analyser sees. The centreline distance to the point where the soot profile rapidly decreases is therefore the best CFD estimate of the flame length. Comparison of figure 5b) with the image analysis shows the agreement is good. The predicted centreline temperature, figure 7, remains high after the end of the visible flame and is therefore not a reliable indicator.

Figure 5c) shows the soot number density profile for the calculation using the simple jet source. As expected, the flame lift-off is less than the experimental observation, although the flame trajectory and visible length show good agreement. The simpler source term also gives a flatter trajectory and less jet spreading than the full shock calculation.

8.4. External radiation

The maximum soot volume fraction levels are of the order 10^{-8} , and are too low to significantly contribute to the external heat radiation. This is reflected in the external radiation calculations which show that the water vapour and carbon dioxide are solely responsible for the recorded intensities. Table 2. shows the positions of 4 radiometers with the measured and predicted incident fluxes. There is little variation between the predicted fluxes from either calculation which compare well with measurements.

9. CONCLUSIONS

1. We have successfully modelled the shock structure for a high pressure natural gas release. This provides an accurate source term necessary for the jet lift-off prediction and downstream combustion.
2. The predicted soot profiles, particularly length, correspond well with the experimental visible flame.
3. Flame trajectory, soot concentrations and external radiation all show good agreement with experiment.
4. The successful validation of the CFD package makes it a powerful tool in the future of hazard consequence modelling.

10. REFERENCES

1. FLOW3D Release 3.3, 1994, User Manual, CFD Department AEA Industrial Technology, and C. Hesketh and P.W. Guilbert, 1989, "RAD3D user manual Version 1.2", AERE-R 13710, HCCP/R32/1989.
2. J. N. Davenport, J.F. Bennett, L.T. Cowley and J.J. Rowson, 1991, "Large-scale natural gas and LPG jet fires. Final report to the CEC", TNER 91, publ. Shell Research Ltd.
3. D. Bradley, P.H. Gaskell and A.K.C. Lau, 1990, "A mixedness-reactedness flamelet model for turbulent diffusion flames", 23rd Symposium on Combustion, pp. 685-692.
4. B. Rogg, 1993, "RUN-1DL. The Cambridge Universal Laminar Flame Code. Version 11.1".
5. R.J. Kee, F.M. Rupley and J.A. Miller, 1991, "CHEMKIN-II: A fortran chemical kinetics package for the analysis of gas phase chemical kinetics", Sandia Report SAND89-8009B.
6. N. Peters, 1984, "Laminar diffusion flamelet models in non-premixed turbulent combustion", Prog. Energy and Combust. Sci., 10, pp. 319-339.
7. D.L. Baulch, C.J. Cobos, R.A. Cox, C. Esser, P. Frank, Th Just, J.A. Ferr, M.J. Pilling, J. Troe, R.W. Walker and J. Warnatz, 1992, "Evaluated kinetic data for combustion modelling", J. Phys. Chem. Ref. Data, 21, no.3, pp411-429.
8. R.W. Bilger, 1988, "The structure of turbulent non-premixed flames", 22nd Int. Symp. on Comb., pp 475-488.
9. X. J. Gu, 1994, Ph.D thesis, Leeds University.
10. D. Bradley, P. H. Gaskell and X. J. Gu, 1994, "Applications of a Reynolds Stress, stretched flamelet, mathematical model to computations of turbulent burning velocities and comparison with experiments", Comb. and Flame 96:221-248.
11. M. Fairweather, W.P. Jones and R.P. Lindstedt, 1992, "Predictions of radiative heat transfer from a turbulent reacting jet in a cross-wind", Combustion and flame, 89, p 45.
12. K.M. Leung, R.P. Lindstedt and W.P. Jones, 1991, "A simplified reaction mechanism for soot formation in nonpremixed flames", Comb. and Flame, 87, pp 289-305.
13. K.B. Lee, M.W. Thring, J.M. Beer, 1962, Combustion and Flame, 6, p137.
14. F.C. Lockwood and N.G. Shah, 1981, "A new radiation solution method for incorporating in general combustion prediction procedures", 18th Int. Symp. on Comb., p1405.
15. D.K. Edwards and A. Balakrishnan, "Thermal radiation by combustion gases", Int. J. Heat Mass Transfer, Vol. 6, p25-40.
16. R.D. Cess, and S. N. Tiwari, 1972, "Infrared radiative energy transfer in gases", Advances in Heat Transfer, Vol. 8, pp. 229-283.

17. R. M. Goody, and M. J. S. Belton, 1967, "Radiative relaxation times for Mars (Discussion of Martian Atmospheric Dynamics)", Planet Space Sci., Vol. 15, no. 2, pp. 247-256.
18. N. L. Crauford, S. K. Liew and J. B. Moss, 1985, Combust. Flame 61: 63-77.
19. A.D. Birch, D.R. Brown, M.G. Dodson and F. Swaffield, 1984, "The Structure and Concentration Decay of High Pressure Jets of Natural Gas". Comb. Sci. Tech., 36, pp 249-261.

Table 1. Flow conditions at orifice and at atmospheric downstream plane

	Conditions at the Orifice used for the full shock calc.	Conditions for the inlet patch at the downstream plane
Pressure (bara)	36.6	1.0
Velocity (m/s)	394.4	429.6
Temperature (K)	244.6	286.0
Jet diameter (m)	0.02	0.128
Mass Flow Rate (kg/s)	3.8	3.8

Table 2. External thermal radiation heat fluxes

Downstream distance (m)	Cross-stream distance (m)	Height above ground (m)	Measured flux kW/m ²	Predicted flux kW/m ²
15	10	1	9.5	9.6
15	14	1	5.8	5.5
15	18	1	3.8	3.4
15	22	1	2.6	2.3

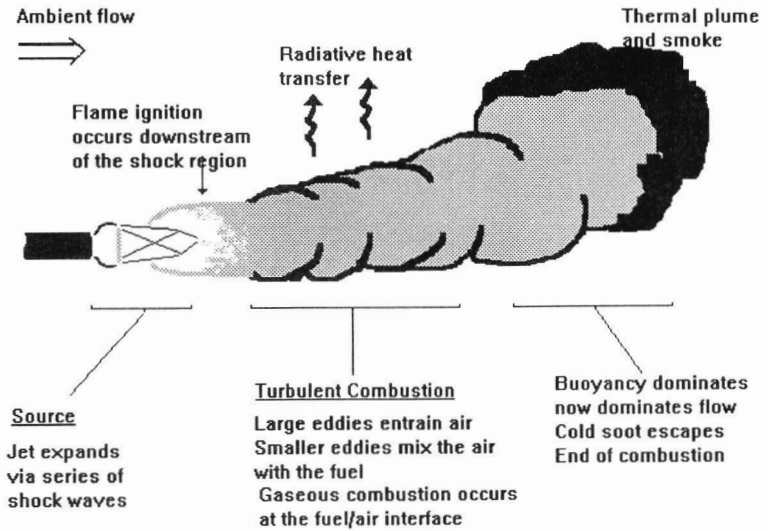


Figure 1. Schematic of a jet fire

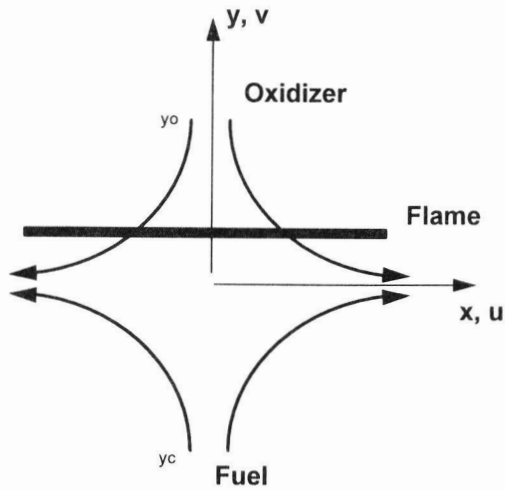


Figure 2. Counter flow laminar diffusion flame. The flame brush sits on the oxidizer side of the stagnation point. The strain rate is defined as $s = \partial u / \partial x$.

Planar Strained Counterflow flame profiles
Run1d1 calculations - C2 chemistry

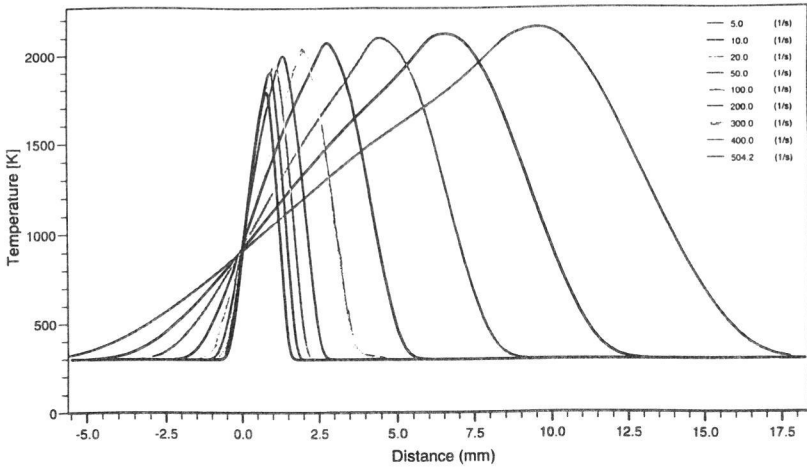


Figure 3. Temperature profiles along the y-axis for counterflow laminar flamelets. As the strain rate increases the width of the flame decreases and the position of the flame moves nearer to the fuel side.

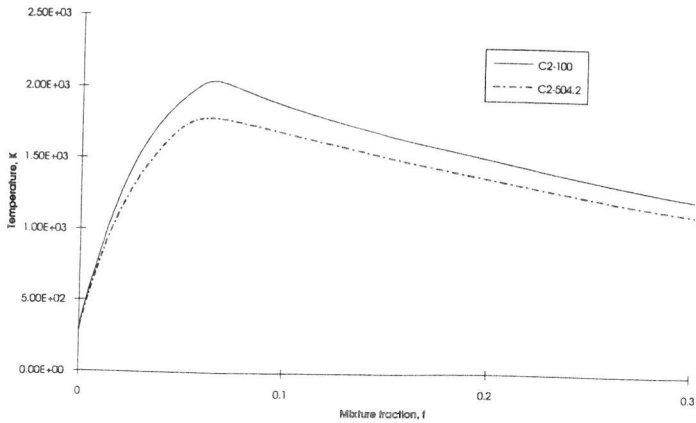


Figure 4. Temperature profiles for planar counterflow geometry at two different strain rates, 100/s and 504.2/s.

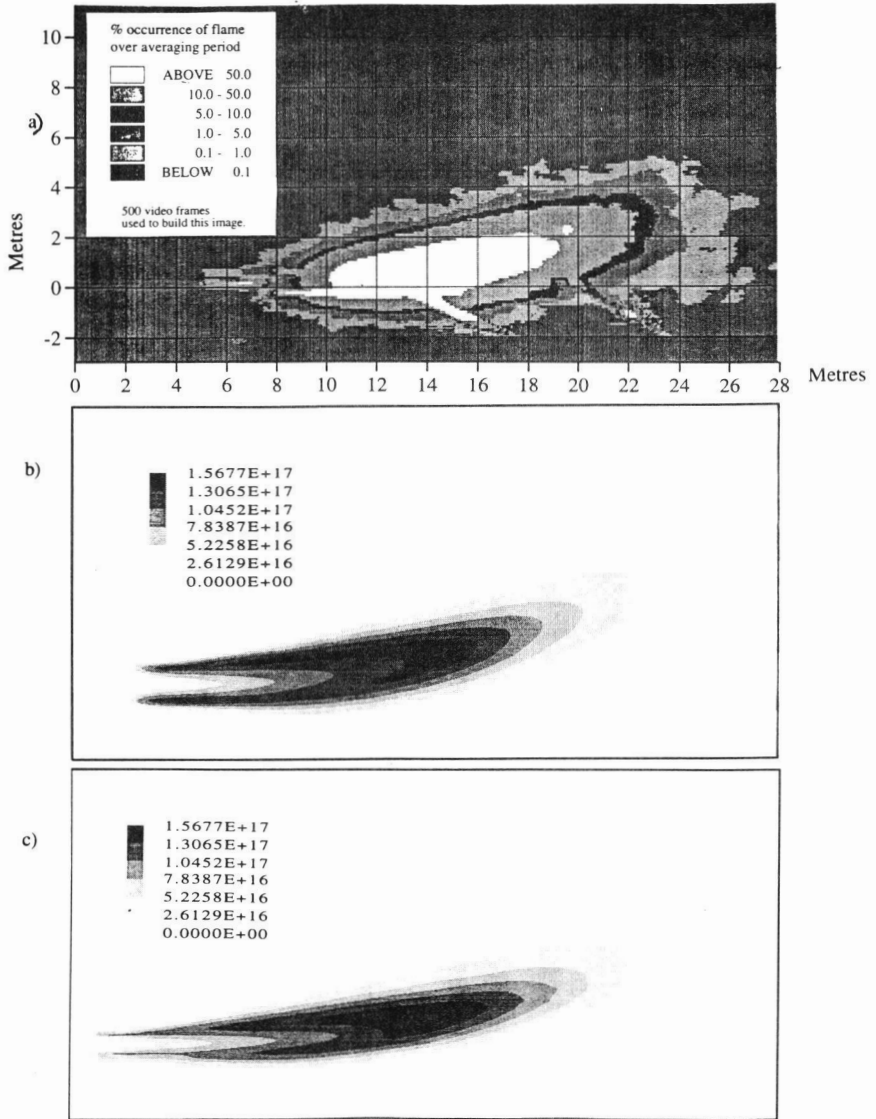


Figure 5a) shows the experimental percentage occurrence map (soot footprint) for the 67.1 bar sonic natural gas flame over a 20 second period, b) Soot number density N , after calculating the initial jet expansion and shock structure, c) Soot number density N , when using the simple jet source expansion of Birch, Brown *et al.* The scale in a) is used for all 3 pictures.

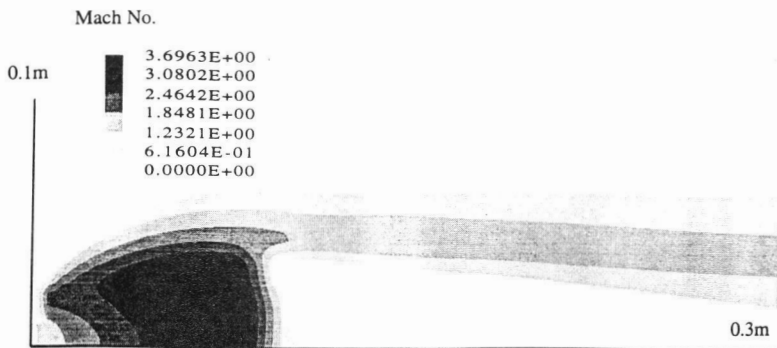


Figure 6. Half slice of the Mach No. profile close to the nozzle during the expansion of the high pressure jet. Reflect about bottom line for full picture

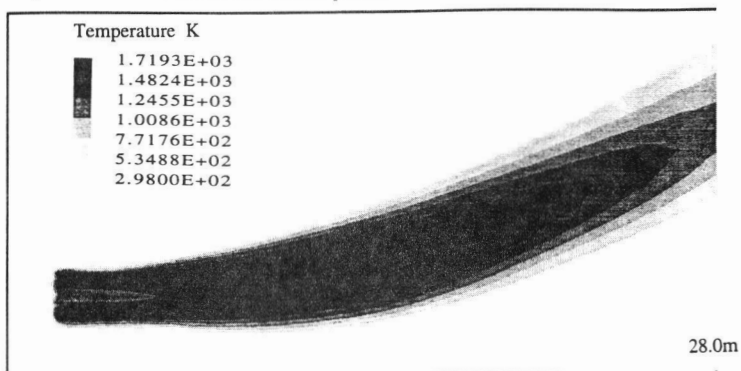


Figure 7. Centreline temperature predictions following the full shock calculation. The flame lift-off is clearly visible.

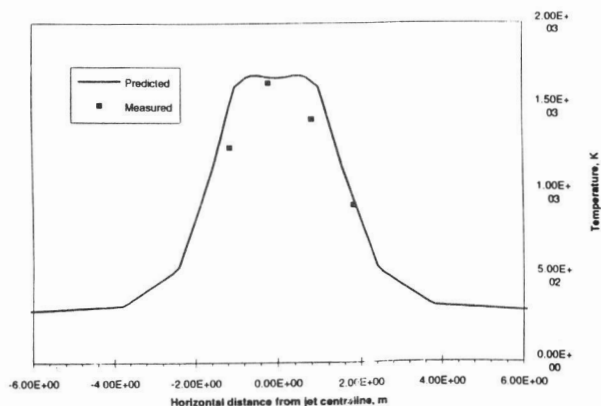


Figure 8. 3.8 kg/s sonic natural gas release - temperature profile 13.6m downstream from release.